# Lande subtraction method with finite integration limits and application to strong-field problems

Tsin-Fu Jiang[*] and Shih-Da Jheng

*Institute of Physics, National Chiao-Tung University, Hsinchu 30010, Taiwan*

Yun-Min Lee[†] and Zheng-Yao Su

*Scientific Computing Division, National Center for High-Performance Computing, R & D Road VI, Hsinchu 30076, Taiwan*

The Lande subtraction method has been widely used in Coulomb problems, but the momentum coordinate $p \in (0, \infty)$ is assumed. In past applications, a very large range of $p$ was used for accuracy. We derive the supplementary formulation with $p \in (0, p_{max})$ at reasonably small $p_{max}$ for practical calculations. With the recipe, accuracy of the hydrogenic eigenspectrum is dramatically improved compared to the ordinary Lande formula by the same momentum grids. We apply the present formulation to strong-field atomic above-threshold ionization and high-order harmonic generations. We demonstrate that the proposed momentum space method can be another practical theoretical tool for atomic strong-field problems in addition to the existing methods.

## I. INTRODUCTION

In solving problems with the Coulomb interaction in momentum space ($\mathcal{P}$-space) [1,2], a singularity in the Coulomb kernel will cause numerical trouble. The difficulty happens in Schrödinger, Dirac, Bethe-Salpeter, and Klein-Gordan equations, and so on. Lande invented a subtraction method and regularized the singularity [3]. The subtraction has been widely adopted in related problems. For instance, Norbury *et al.* [4] applied a specific form of basis function for the bound states, and Tang *et al.* [5] used the Bystrom method for the Coulomb-kernel-related integration and solved some bound states. Recently, multiphoton ionization processes for intense laser on hydrogen atom were extensively studied by using the Lande subtraction in a time-dependent Schrödinger equation [6].

In the Lande subtraction formulation [3,7], the range of momentum is $p \in (0, \infty)$. Thus, we can see why in previous applications of Lande's method, $p_{max}$ up to several thousands atomic units was used to mimic $p_{max} \sim \infty$, otherwise the eigenstates cannot be calculated accurately enough. But $p^2/2$ is the order of particle kinetic energy. Such a large momentum requires a large number of grids for fine energy resolution. The $\mathcal{P}$-space method is becoming useful, because with the progress being made in measurement techniques, there are more and more photoelectron experiments [8,9]. The photoionized electron is described by a wave packet consisting of continuous states. In coordinate space ($\mathcal{R}$-space), these states extend to large distances. However, they are always localized in $\mathcal{P}$-space and can be handled. So, the $\mathcal{P}$-space method will be a good tool for current research of laser pulses on atoms or molecules.

In this work, we derive the supplementary formulation when a moderate $p_{max}$ is used in the Lande subtraction method. Thus, the application of the Lande method is then no longer limited by the large $p_{max}$ and becomes tractable numerically. With this recipe, a few hundred grids with $p_{max}$ around several tens of a.u., satisfactory accurate eigenspectra can be generated.

More grids and larger but still moderate $p_{max}$ generate a highly accurate eigenset. The result, with dramatic improvement compared to the ordinary Lande formula, is shown. We apply the new formulation to quantum dynamics of an atom under intense laser pulse; both high-order generations (HHG) and above-threshold ionization (ATI) spectra are obtained in one calculation. Usually, the electron spectra can be calculated by solving the time-dependent Schrödinger equation in $\mathcal{R}$-space. But this method is often limited by reflection of wave function from the numerical boundary during the laser excitation. A large spatial region must be used such that the electron wave function is always away from the numerical boundary during the laser pulse. The computer memory and CPU time will then be demanding and even unfeasible for stronger intensity or a longer pulse. Previously, we developed methods using the momentum wave functions as a basis set to study atom in laser fields, and we were able to bypass the trouble of boundary reflection. We have shown that the low-order ATI phenomenon is described rather well by the momentum space method [10,11]. The current method is more accurate and efficient than our previous methods using the finite momentum grid formulation of the Lande subtraction method.

The rest of the paper is organized as follows. In Sec. II, we derive the formulation of finite $p_{max}$ using the Lande subtraction method. In Sec. III, the eigenstates of hydrogen atom from the present formulation and ordinary Lande subtraction method are compared. We also discuss this method applied to helium atom. In Sec. IV, we describe the time-dependent method with applications to HHG and ATI of intense laser pulse on hydrogen atom. We present the separate contributions to HHG for transitions from continuous-to-bound states, continuous-to-continuous states, and bound-to-bound states. Conclusions are drawn in Sec. V.

## II. SUPPLEMENTARY FORMULATION OF FINITE MOMENTUM TO ORDINARY LANDE SUBTRACTION METHOD

Consider the eigenvalue equation of a spherical symmetric potential $V(r)$ in the $\mathcal{R}$-space representation

$$-\tfrac{1}{2}\nabla^2\Psi(\vec{r}) + V(r)\Psi(\vec{r}) = E\Psi(\vec{r}) \tag{1}$$

---

[*]Corresponding author: tfjiang@faculty.nctu.edu.tw

[†]Current address: Department of Mechanical Engineering, National Chiao-Tung University, Hsinchu 30010, Taiwan.

by making the Fourier transformation

$$\Phi(\vec{p}) = 1/(2\pi)^{\frac{3}{2}} \int \Psi(\vec{r}) e^{-i\vec{p}\cdot\vec{r}} d^3r \,,$$

$$W(\vec{p}) = 1/(8\pi^3) \int V(\vec{r}) e^{-i\vec{p}\cdot\vec{r}} d^3r \,. \tag{2}$$

The corresponding $\mathcal{P}$-space representation becomes [2,12,13]

$$\left[\frac{p^2}{2} - E\right]\Phi(\vec{p}) + \int W(\vec{p} - \vec{q})\Phi(\vec{q})d^3q = 0. \tag{3}$$

Specifically for the hydrogenic Coulomb potential $V(\vec{r}) = -Z/r$, we have $W(\vec{p}) = -Z/(2\pi^2 p^2)$. We designate the spherical symmetric eigenstates as

$$\Phi_{nlm}(\vec{p}) = F_{nl}(p)Y_{lm}(\Omega_p) \,, \tag{4}$$

and the eigenvalue equation is then reduced to radial only,

$$\left[\frac{p^2}{2} - E\right]F_{nl}(p) + \int q^2 K_l(p,q)F_{nl}(q)dq = 0. \tag{5}$$

The Coulomb kernel $K_l$ in the above equation can be expressed in terms of the second kind of Legendre function, $Q_l$,

$$K_l(p,q) = -\frac{Z}{\pi p q} Q_l\left(\frac{p^2 + q^2}{2pq}\right), \tag{6}$$

with

$$Q_l(z) = \frac{1}{2}\int_{-1}^{1} \frac{1}{z - x} P_l(x)dx, \tag{7}$$

where $P_l$ is the first kind of Legendre function. Some analytic solutions of the hydrogen eigenstates in $\mathcal{P}$ space were given in Refs. [12,13]. Direct numerical solution of the equation is not straightforward due to the singularity in $Q_l(z)$ when $z = (p^2 + q^2)/(2pq) = 1$ or, equivalently, when $p = q$. Lande proposed a regularization method to manipulate the kernel term as follows [3]:

$$\int q^2 K_l(p,q)F_{nl}(q)dq$$

$$= \int K_l(p,q)[q^2 F_{nl}(q) - p^2 F_{nl}(p)/P_l(z)]dq$$

$$+ p^2 F_{nl}(p)\int \frac{K_l(p,q)}{P_l(z)}dq. \tag{8}$$

The first term on the right-hand side is now vanishing at $z = 1$ (that is, $p = q$), and the last term is finite and can be calculated iteratively from $l = 0$, if the range of momentum $p$ is zero to infinity [3,7]. This is the *ordinary* adopted Lande subtraction formulation, with $p \in (0,\infty)$ understood.

In a practical calculation, $p \in (0,p_{\max})$ with a moderate value of $p_{\max}$ is anticipated. We cast the last term in the above equation into

$$p^2 \int_0^{p_{\max}} \frac{K_l(p,q)}{P_l(z)}dq = \frac{-pZ}{\pi}\int_0^{p_{\max}} \frac{Q_l(z)}{q P_l(z)}dq \equiv -pZ J_l(p),$$

with

$$Q_l(z) = \frac{1}{2}P_l(z)\ln\frac{z + 1}{z - 1} - W_{l-1}(z), \quad z = \frac{p^2 + q^2}{2pq},$$

and

$$W_{l-1}(z) = \sum_{k=1}^{l} \frac{1}{k} P_{k-1}(z) P_{l-k}(z).$$

So we have

$$J_l(p) = \frac{1}{2\pi}\int_0^{p_{\max}} \ln\frac{z + 1}{z - 1}\frac{dq}{q} - \frac{1}{\pi}\int_0^{p_{\max}} \frac{W_{l-1}(z)}{P_l(z)}\frac{dq}{q}. \tag{9}$$

The first term in $J_l(p)$ is found to be

$$\frac{1}{2\pi}\int_0^{p_{\max}} \ln\frac{z + 1}{z - 1}\frac{dq}{q}$$

$$= \frac{1}{2\pi}\int_0^{p} + \frac{1}{2\pi}\int_p^{p_{\max}},$$

$$= \frac{1}{\pi}\int_0^{p} \ln\frac{p + q}{p - q}\frac{dq}{q} + \frac{1}{\pi}\int_p^{p_{\max}} \ln\frac{p + q}{q - p}\frac{dq}{q},$$

$$= \frac{1}{\pi}\int_0^{1} \ln\frac{1 + x}{1 - x}\frac{dx}{x} + \frac{1}{\pi}\int_s^{1} \ln\frac{1 + x}{1 - x}\frac{dx}{x},$$

$$= \frac{2}{\pi}\int_0^{1} \frac{dx}{x}\tanh^{-1}(x) + \frac{2}{\pi}\int_s^{1} \frac{dx}{x}\tanh^{-1}(x),$$

$$= \frac{\pi}{2} - \frac{2}{\pi}\left[s + \frac{s^3}{3^2} + \frac{s^5}{5^2} + \frac{s^7}{7^2} + \cdots\right], \tag{10}$$

where $s = p/p_{\max}$ [14]. We sum the series until the highest-order term is less than a small number $\epsilon$. Since the interior grids of $p$ are used, $s$ is always less than 1 and the criterion works. The number of terms $n$ summed can be found by solving $s^{2n+1}/(2n + 1)^2 = \epsilon$. In the simulation, we used $p_{\max} = 100$ a.u. and $\epsilon = 10^{-9}$. For $s = 0.1$, a sum of 5 terms was needed, $s = 0.5$ needed 12 terms, $s = 0.9$ needed 59 terms, and $s = 0.99$ required 385 terms. The second term in $J_l(p)$ is regular and can be calculated by numerical quadrature. Note that (i) instead of simply equal to $\pi/2$ with $p_{\max} = \infty$ in the first term, there is an important correction term, $-\frac{2}{\pi}[s + \frac{s^3}{3^2} + \frac{s^5}{5^2} + \frac{s^7}{7^2} + \cdots]$, to the ordinary Lande formula with $p_{\max} = $ finite. The correction is a function of $p$. (ii) The second term in $J_l(p)$ is now integrated from $(0,p_{\max})$, not $(0,\infty)$. Together with the integration of the first term in the right-hand side of Eq. (8) with $p \in (0,p_{\max})$, we arrive at the *supplementary* formulation of the Lande subtraction method with a finite range of momentum.

To elucidate the improvement of eigenstates by this supplementary formulation to the ordinary Lande subtraction formula, we present in Table I the results of hydrogen atom. We employ the term *Present* to denote that $p \in (0,p_{\max})$ is used, as in Eq. (8), and *Ordinary* to denote that the analytical form $p \in (0,\infty)$ is used, such as derived in Refs. [3,7].

In the latter case, the range of momentum can be as large as possible but never $\infty$ numerically. In the table, we list (a) the deviation of some energy levels and (b) the corresponding root-mean-square deviation of the wave functions $\Delta\Phi$,

TABLE I. Comparisons of results from Present method and the Ordinary Lande formula. $[E(nl) - \text{exact}]$ is the deviation of energy levels for the first few low-lying states. $\Delta\Phi$ is the root-mean-square deviation of the wave function. The corresponding exact $\mathcal{P}$-space wave functions are from Ref. [13]. Case I denotes that 2048 grids and $p_{\max} = 100$ a.u. are used, and case II that 2048 grids and $p_{\max} = 2000$ a.u., $1.76(-6) \equiv 1.76 \times 10^{-6}$.

| State | (I) $E(nl) - \text{exact}$ | | (I) $\Delta\Phi$ | | (II) $E(nl) - \text{exact}$ | | (II) $\Delta\Phi$ | |
|---|---|---|---|---|---|---|---|---|
| (nl) | Present | Ordinary | Present | Ordinary | Present | Ordinary | Present | Ordinary |
| $1s$ | $1.76(-6)$ | $-6.45(-3)$ | $6.90(-8)$ | $2.45(-4)$ | $7.77(-8)$ | $-3.18(-4)$ | $5.99(-10)$ | $1.22(-5)$ |
| $2s$ | $2.75(-7)$ | $-1.61(-3)$ | $6.88(-8)$ | $4.25(-4)$ | $6.55(-8)$ | $-7.96(-5)$ | $1.01(-9)$ | $2.11(-5)$ |
| $3s$ | $1.24(-7)$ | $-7.16(-4)$ | $6.88(-8)$ | $6.17(-4)$ | $6.25(-8)$ | $-3.53(-5)$ | $1.41(-9)$ | $3.07(-5)$ |
| $2p$ | $-1.56(-10)$ | $-4.14(-8)$ | $1.01(-10)$ | $1.34(-8)$ | $-1.78(-10)$ | $-4.95(-10)$ | $4.39(-9)$ | $1.90(-10)$ |
| $3p$ | $-8.75(-10)$ | $-1.83(-8)$ | $6.46(-10)$ | $1.84(-8)$ | $-9.45(-10)$ | $-1.06(-9)$ | $6.85(-8)$ | $7.69(-10)$ |
| $3d$ | $2.38(-10)$ | $2.38(-10)$ | $4.21(-10)$ | $4.22(-10)$ | $3.86(-10)$ | $2.70(-10)$ | $7.66(-8)$ | $5.58(-10)$ |

defined as

$$\Delta\Phi = \sqrt{\frac{1}{N} \int |\Phi(\vec{p}) - \Phi_{\text{exact}}(\vec{p})|^2 d^3 p}, \qquad (11)$$

where $N$ is the number of $p$ grids, $\Phi(\vec{p})$ is calculated, and $\Phi_{\text{exact}}(\vec{p})$ is the exact momentum-space wave function. The analytic forms of the first few low-lying states are listed in Ref. [13]. Among the eigenstates, the ground state is equal to

$$F_{1s} = \frac{2^{5/2}}{\sqrt{\pi}} \frac{1}{(p^2 + 1)^2}, \qquad (12)$$

which is the most diffusive state and needs a larger $p_{\max}$ to attain higher accuracy. The best accuracy can be reached is $\sim 1/[p_{\max}]^4$ theoretically. To check the effects of $p_{\max}$, we present two cases, with (i) $N = 2048$ and $p_{\max} = 100$ a.u. and (ii) $N = 2048$ and $p_{\max} = 2000$ a.u. In both cases, the errors of the $1s$ and $2s$ eigenvalues and wave function deviations by use of the Present formulation are about 3 orders of magnitude smaller than the Ordinary ones (also because the accuracy limit of $F_{1s}(p)$ is $\sim p_{\max}^{-4}$). We can see that the highest possible accuracy is reached by use of the Present method. Even with a quite large value, $p_{\max} = 2000$, the Ordinary results are still far worse than those of the supplementary formulation presented here. For other higher states, the wave functions $F_{nl}(p)$ are rather localized in smaller $p$, and, hence, the improvement is not as dramatic as with the $1s$ and $2s$ states. However, the Present results are highly accurate even with $p_{\max} = 100$ a.u. For example, with 512 grids and $p_{\max} = 100$ a.u., the Present method generates comparable accuracy compared to the Ordinary method with 2048 grids and $p_{\max} = 2000$ a.u. in Table. I. But the Hamiltonian matrix is $512 \times 512$ compared to $2048 \times 2048$. So the Present method is more efficient than the Ordinary method, especially for the time-dependent problems. With even smaller value of $p_{\max}$, the spectrum is also reliable with a bit of a sacrifice of accuracy for $1s$ and $2s$, but the Ordinary results cannot be trusted. The Present scheme with small $p_{\max}$ ensures that the strong field dynamics can be investigated in momentum space. So, the numerical improvement introduced here through the supplementary formulation of the Lande subtraction method is important.

We use hydrogen atom as a calibration mainly due to the exact energy levels and the fact that some momentum wave functions are analytically known. The method is applicable

to general single-active electron (SAE) atoms, too. As an example, we study the helium atom by SAE1 [15] and SAE2 [16] model potentials. The SAE1 model potential uses a Slater-type basis and is optimized to the accurate ground state. It is parameterized as

$$V(r) = -\frac{1}{r} - \frac{\sum_{p=0}^{2} \sum_{k=1}^{2} c_{k,p} \, r^p \, e^{-\beta_{k,p} r}}{r}, \qquad (13)$$

with $c_{1,0} = 0.3374$, $c_{2,0} = 0.6626$, $\beta_{1,0} = 6.2838$, $\beta_{2,0} = 0.2382$, $c_{1,1} = 1.6724$, $c_{2,1} = -1.1558$, $\beta_{1,1} = 3.6076$, $\beta_{2,1} = 1.3969$, $c_{1,2} = -1.1088$, $c_{2,2} = -0.3320$, $\beta_{1,2} = 3.6418$, and $\beta_{2,2} = 0.8108$.

The SAE2 model potential fits the first few low-lying states to experimental data. The potential is written as

$$V(r) = -\frac{1}{r} - \frac{a_1 e^{-a_2 r} + a_3 r e^{-a_4 r} + a_5 e^{-a_6 r}}{r}, \qquad (14)$$

with parameters for helium atom, $a_1 = 1.231$, $a_2 = 0.662$, $a_3 = -1.325$, $a_4 = 1.236$, $a_5 = -0.231$, and $a_6 = 0.480$. Both model potentials keep correct behaviors at $r \to 0$ and $r \to \infty$. They have identical long-ranged parts but differ in the inner region. In Fig. 1 we plot $r$ times the short-ranged potential and their difference. We apply the Present method to both potentials. The Fourier transform of the SAE1 potential
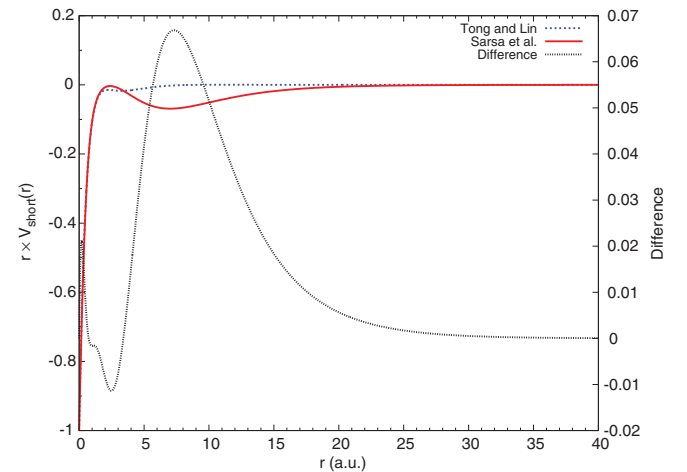


FIG. 1. (Color online) The $r \times V_{\text{short-ranged}}(r)$ of SAE1 (red solid line) and SAE2 (dashed blue line) and their difference (dotted black line, labeled in the right vertical axis).

TABLE II. Differences of helium atom energy levels from the Present $\mathcal{P}$-space method and the $\mathcal{R}$-space method for SAE1 and SAE2. The $\mathcal{R}$-space energy levels are accurate up to machine precision. Case I denotes 1024 grids with $p_{\max} = 50$ a.u., case II for 1024 grids with $p_{\max} = 100$ a.u., case III for 2048 grids with $p_{\max} = 50$ a.u., and case IV for 2048 grids with $p_{\max} = 100$ a.u. $2.44(-3) \equiv 2.44 \times 10^{-3}$. Atomic units are used.

| State and model | Case I | | Case II | | Case III | | Case IV | |
|---|---|---|---|---|---|---|---|---|
| | SAE1 | SAE2 | SAE1 | SAE2 | SAE1 | SAE2 | SAE1 | SAE2 |
| $1s$ | 2.44(−3) | 2.14(−3) | 2.24(−3) | 1.94(−3) | 1.38(−3) | 1.21(−3) | 1.15(−3) | 9.90(−4) |
| $2s$ | 2.23(−4) | 2.63(−4) | 3.13(−4) | 2.52(−4) | 1.71(−4) | 1.41(−4) | 1.58(−4) | 1.27(−4) |
| $3s$ | 1.51(−4) | 9.27(−5) | 1.48(−4) | 9.01(−5) | 7.80(−5) | 4.88(−5) | 7.44(−5) | 4.53(−5) |
| $2p$ | 1.09(−4) | 2.58(−5) | 1.10(−4) | 2.62(−5) | 5.33(−5) | 1.29(−5) | 5.40(−5) | 1.31(−5) |
| $3p$ | 5.65(−5) | 9.81(−6) | 5.72(−5) | 9.95(−6) | 2.78(−5) | 4.91(−6) | 2.81(−5) | 4.98(−6) |
| $3d$ | 6.06(−5) | 1.91(−6) | 6.14(−5) | 1.94(−6) | 3.05(−5) | 9.58(−7) | 3.08(−5) | 9.70(−7) |

is

$$W(\vec{p}) = -\frac{1}{2\pi^2 p^2} - \frac{1}{2\pi^2} \left\{ \frac{c_{1,0}}{\beta_{1,0}^2 + p^2} + \frac{c_{2,0}}{\beta_{2,0}^2 + p^2} \right.$$
$$+ \frac{2c_{1,1}\beta_{1,1}}{\left(\beta_{1,1}^2 + p^2\right)^2} + \frac{2c_{2,1}\beta_{2,1}}{\left(\beta_{2,1}^2 + p^2\right)^2} + \frac{2\left(3c_{1,2}^2 - p^2\right)}{\left(\beta_{1,2}^2 + p^2\right)^2}$$
$$\left. + \frac{2\left(3c_{2,2}^2 - p^2\right)}{\left(\beta_{2,2}^2 + p^2\right)^2} \right\}, \quad (15)$$

and the Fourier transform of the SAE2 potential is

$$W(\vec{p}) = -\frac{1}{2\pi^2 p^2}$$
$$- \frac{1}{2\pi^2} \left\{ \frac{a_1}{a_2^2 + p^2} + \frac{2a_3 a_4}{\left(a_4^2 + p^2\right)^2} + \frac{a_5}{a_6^2 + p^2} \right\}. \quad (16)$$

Since the analytical results are unknown, we calculate the $\mathcal{R}$-space eigenvalue equation accurately by use of the generalized pseudospectral (GPS) method [17] for calibration. In Table II, we list the energy level differences of the present $\mathcal{P}$-space method and the $\mathcal{R}$-space GPS results for each model potential for the first few low-lying states with four calculations as follows: (case I) 1024 grid points in p with $p_{\max} = 50$ a.u., (case II) 1024 grids with $p_{\max} = 100$ a.u., (case III) 2048 grids with $p_{\max} = 50$ a.u., and (case IV) 2048 grids with $p_{\max} = 100$ a.u. We can see that the improvement of $1s$ energy is not as dramatic as hydrogen atom. But the $\mathcal{P}$-space eigenstates are generally acceptable to give a good representation for each individual SAE potential.

## III. TIME-DEPENDENT METHOD IN MOMENTUM SPACE

### A. Split-operator algorithm for time propagation

The momentum space time-dependent Schrödinger equation ($\mathcal{P}$-TDSE) of an SAE atom in a laser pulse under the dipole approximation can be written as

$$i\frac{\partial \Psi_{\text{total}}}{\partial t} = \left[ H_0 + \vec{p} \cdot \vec{A}(t) + \frac{1}{2}A^2(t) \right] \Psi_{\text{total}}(\vec{p},t), \quad (17)$$

with the electric field $\vec{E}(t) = -\partial \vec{A}(t)/\partial t$. For a linearly polarized field, the magnetic quantum number $m$ is a good quantum number during the laser pulse and, hence, is omitted

for convenience. By making the transform

$$\Psi_{\text{total}}(\vec{p},t) = \exp\left\{ \frac{-i}{2} \int_{-\infty}^{t} A^2(t')dt' \right\} \Psi(\vec{p},t), \quad (18)$$

$\Psi(\vec{p},t)$ then satisfies the following $\mathcal{P}$-TDSE:

$$i\frac{\partial \Psi}{\partial t} = [H_0 + \vec{p} \cdot \vec{A}(t)]\Psi(\vec{p},t). \quad (19)$$

$H_0$ is the Hamiltonian operator of the SAE atom, and

$$H_0 \Psi(\vec{p},t) = \frac{p^2}{2}\Psi(\vec{p},t) + \int W(\vec{p} - \vec{q})\Psi(\vec{q},t)d^3q. \quad (20)$$

The split-operator algorithm [18] is used for the time propagation,

$$\Psi(\vec{p},t+\Delta) = e^{-iH_0\frac{\Delta}{2}} e^{-i\vec{p}\cdot\int_t^{t+\Delta}\vec{A}(t')dt'} e^{-iH_0\frac{\Delta}{2}} \Psi(\vec{p},t) + O(\Delta^3). \quad (21)$$

In each time step, define, first,

$$\Psi^{(1)}(\vec{p},t) = e^{-iH_0\frac{\Delta}{2}} \Psi(\vec{p},t) \quad (22)$$

and use the eigenstates solved by the method in previous section as energy representation of the operator $e^{-iH_0\frac{\Delta}{2}}$,

$$\Psi^{(1)}(\vec{p},t) = \sum_{n,l} \Phi_{n,l}(\vec{p})e^{-iE_{n,l}\frac{\Delta}{2}} \int \Phi_{n,l}^*(\vec{q})\Psi(\vec{q},t)d^3q, \quad (23)$$

where

$$H_0 \Phi_{n,l}(\vec{p}) = E_{n,l}\Phi_{n,l}(\vec{p}), \quad \text{and} \quad \int |\Phi_{n,l}(\vec{p})|^2 d^3p = 1. \quad (24)$$

Expand $\Psi(\vec{q},t) = \sum_k f_k(q)Y_{k,m}(\hat{q})$ and define $\Psi^{(1)}(\vec{p},t) = \sum_l \Psi_l^{(1)}(p)Y_{l,m}(\hat{p})$; we then have

$$\Psi_l^{(1)}(p) = \int S^{(l)}(p,q)f_l(q)q^2 dq,$$

where

$$S^{(l)}(p,q) = \sum_n \Phi_{n,l}(p)e^{-iE_{n,l}\frac{\Delta}{2}}\Phi_{n,l}(q). \quad (25)$$

In grid representation, the matrix $S^{(l)}(p_i,p_j)$ is time independent and we need to calculate only one time for each angular momentum $l$.

Next we designate

$$
\begin{aligned}
\Psi^{(2)}(\vec{p},t) &= e^{-i\vec{p}\cdot\int_t^{t+\Delta}\vec{A}(t')dt'}\Psi^{(1)}(\vec{p},t), \\
&= e^{-i\vec{p}\cdot\vec{\alpha}(t,\Delta)}\Psi^{(1)}(\vec{p},t),
\end{aligned}
$$

with

$$
\vec{\alpha}(t,\Delta) = \int_t^{t+\Delta}\vec{A}(t')dt'. \tag{26}
$$

The propagation is in angular momentum subspace for each grid $p_i$ [6]. Let $\vec{p}\cdot\vec{\alpha} \equiv p\alpha\cos\theta$. We, first, diagonalize $\hat{K} = \cos\theta$ in the $\{Y_{l,0}(\theta)\}$ basis, namely

$$
\hat{K}\chi_k(l) = \lambda_k\chi_k(l), \quad k,l = 0,1,2,\ldots,L. \tag{27}
$$

Then, with $\Psi^{(2)}(\vec{p},t) \equiv \sum_l g_l(p,t)Y_{l,0}(\hat{p})$,

$$
g_l(p_i,t) = \sum_{l'}\Lambda_{l,l'=0}^{l'=L}(p_i,t)f_{l'}(p_i,t),
$$

where

$$
\Lambda_{l,l'}(p_i,t) = \sum_{k=0}^{L}\chi_k(l)e^{-ip_i\alpha(t,\Delta)\lambda_k}\chi_k^*(l'). \tag{28}
$$

Again, the set $\{\lambda_k,\chi_k\}$ is independent of time. Propagation of this step is in $l$ subspace for each grid $p_i$.

In the data presented later, for a hydrogen atom under the Gaussian pulse with full width at half maximum (FWHM) of 5 fs, wavelength 800 nm, and peak intensities 100, 200, 300, and 400 TW/cm$^2$, $L$ are 8, 17, 23, and 28, respectively, such that the contribution to norm from the corresponding highest angular momentum $L$ is less than 0.1%. So, usually a limited number of angular momenta are enough for time evolution. The matrix size of $\Lambda$ is, hence, small and the propagation is quite efficient. The time propagation scheme described above uses the eigenstates $\Phi_{nl}(\vec{p})$ of $H_0$, which need only be calculated one time. Besides the importance of accuracy, smaller size of eigenstates will save much computing time. As an example, for simulations for a 5-fs Gaussian pulse of peak intensity 100 TW/cm$^2$ with 16 angular momenta, the computing time for 512 grids is 3 min and 2 s and for 2048 grids is 74 min and 12 s, respectively. The results in this paper were generated with a desktop personal computer with an Intel i7 CPU with eight threads.

### B. High-order harmonic generations

We decompose the wave function into the continuous and the bound parts at each time step by projection as

$$
\begin{aligned}
\Psi(\vec{p},t) &= \sum_l f_l(p,t)Y_{l,m}(\vec{p}), \\
f_l(p,t) &= \psi_l^{\text{conti}}(p,t) + \psi_l^{\text{bound}}(p,t),
\end{aligned} \tag{29}
$$

where

$$
\begin{aligned}
\psi_l^{\text{bound}}(p,t) &= \sum_{\text{bound }(nl)}F_{nl}(p)\int F_{nl}^*(q)f_l(q,t)q^2dq, \\
\psi_l^{\text{conti}}(p,t) &= f_l(p,t) - \psi_l^{\text{bound}}(p,t)
\end{aligned} \tag{30}
$$

and

$$
\Psi(\vec{p},t) = \Psi^{\text{conti}}(\vec{p},t) + \Psi^{\text{bound}}(\vec{p},t),
$$

with

$$
\begin{aligned}
\Psi^{\text{bound}}(\vec{p},t) &= \sum_l \psi_l^{\text{bound}}(p,t)Y_{l,m}(\vec{p}), \\
\Psi^{\text{conti}}(\vec{p},t) &= \sum_l \psi_l^{\text{conti}}(p,t)Y_{l,m}(\vec{p}),
\end{aligned} \tag{31}
$$

because the system is time varying and the states are field dressed. It is intractable to calculate the dressed states at every time due to the larger number of time steps. So we can make decomposition only approximately. We model states with energy larger than the ponderomotive energy ($U_p$) as continuous and with energy less than $U_p$ as bound. We will see later that this classification of continuous and bound parts is meaningful.

Classically, accelerating charge will emit electromagnetic radiation. Under the linearly polarized light, the acceleration form dipole function is found through

$$
d_A(t) \equiv \langle\Psi(t)|\frac{d^2z}{dt^2}|\Psi(t)\rangle. \tag{32}
$$

By using the velocity $dz/dt = p_z + A(t)$, we can derive the relationship between the velocities from the dipole functions $d_v(t)$ and $d_A(t)$ as follows:

$$
\begin{aligned}
d_v(t) &\equiv \langle\Psi(t)|\frac{dz}{dt}|\Psi(t)\rangle = \langle\Psi(t)|p_z|\Psi(t)\rangle + A(t), \\
\frac{d}{dt}[d_v(t) - A(t)] &= \frac{d}{dt}\langle\Psi(t)|p_z|\Psi(t)\rangle = d_A(t).
\end{aligned} \tag{33}
$$

We then take the Fourier transform for the power spectrum,

$$
\begin{aligned}
\int_{-\infty}^{\infty}d_A(t)e^{-i\omega t}dt &= \int_{-\infty}^{\infty}\frac{d}{dt}\langle p_z\rangle e^{-i\omega t}dt, \\
&= \langle p_z(t)\rangle e^{-i\omega t}|_{-\infty}^{+\infty} + i\omega\int_{-\infty}^{\infty}\langle p_z\rangle e^{-i\omega t}dt.
\end{aligned} \tag{34}
$$

Thus, from the function $\langle p_z(t)\rangle$, the acceleration form HHG power spectrum can be obtained. By the decomposition of total wave function, we have

$$
\begin{aligned}
\langle p_z(t)\rangle = &\langle\Psi^{\text{bound}}(\vec{p},t)|p_z|\Psi^{\text{bound}}(\vec{p},t)\rangle \\
&+ \langle\Psi^{\text{conti}}(\vec{p},t)|p_z|\Psi^{\text{conti}}(\vec{p},t)\rangle \\
&+ \{\langle\Psi^{\text{bound}}(\vec{p},t)|p_z|\Psi^{\text{conti}}(\vec{p},t)\rangle \\
&+ \langle\text{complex conjugate}\rangle\}.
\end{aligned} \tag{35}
$$

In this way, we can study the contributions to the HHG spectrum from bound-bound, continuous-continuous, and continuous-bound transitions separately. While in $\mathcal{R}$-TDSE, usually we filter out the wave function at a larger distance from the nucleus, otherwise the calculation will not be feasible [19]. Hence, in the $\mathcal{R}$-TDSE calculation, the effect of the filtered wave-function contribution to HHG is not considered. In the semiclassical three-step model [20–22], only transitions from continuous states to the ground state are included and the Volkov or Coulomb-Volkov [23,24] approximation is used for the continuous state atomic electron under laser pulse. On the other hand, the $\mathcal{P}$-TDSE method can provide the complete information of HHG spectra.
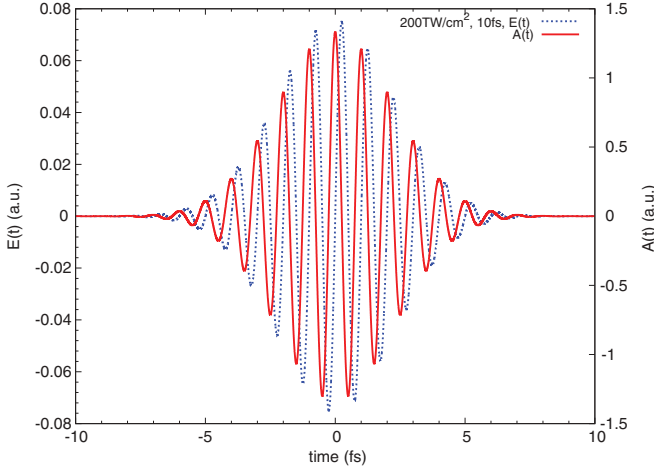
FIG. 2. (Color online) Electric field (dotted blue line) and vector potential (red line) profiles of a Gaussian pulse at peak intensity 200 TW/cm$^2$, FWHM 10 fs, and wavelength 800 nm.

### C. Above threshold ionization spectra

At the end of a laser pulse, we can subtract the bound states from the total final wave function and obtain the continuous part, namely

$$\Psi^{\text{conti}}(\vec{p}, t = \infty) = \Psi(\vec{p}, t = \infty) - \sum_{n_b, l_b} \Phi_{n_b, l_b}(\vec{p})$$
$$\times \int \Phi_{n_b, l_b}^*(\vec{q}) \Psi(\vec{q}, t = \infty) d^3 q, \quad (36)$$

where $\Phi_{n_b, l_b}(\vec{p})$ are bound states of the SAE Hamiltonian, $H_0$. The photoelectron angular distribution (PAD) is conveniently expressed in a two-dimensional momentum plot. Let $p_\parallel$ and $p_\perp$ be the component of momentum $\vec{p}$ in parallel and perpendicular to the polarization axis and $\theta$ the angle between $\vec{p}$ and the polarization axis, and then $p_\parallel = p \cos\theta$, and $p_\perp = \sqrt{p_x^2 + p_y^2} = p \sin\theta$. The ionization probability $\mathcal{P}$ will be expressed as

$$\mathcal{P} \equiv \int \frac{\partial^2 \mathcal{P}}{\partial p_\parallel \partial p_\perp} dp_\parallel dp_\perp,$$

where

$$\frac{\partial^2 \mathcal{P}}{\partial p_\parallel \partial p_\perp} = \int p_\perp |\Psi^{\text{conti}}(\vec{p}, t = \infty)|^2 d\phi. \quad (37)$$

We can also denote the photoelectron spectrum as follows:

$$\mathcal{P} \equiv \int_{\epsilon=0}^{\infty} \frac{\partial \mathcal{P}}{\partial \epsilon} d\epsilon = \int |\Psi^{\text{conti}}(\vec{p}, t = \infty)|^2 d^3 p,$$

where

$$\frac{\partial \mathcal{P}}{\partial \epsilon} = \int\int p|\Psi^{\text{conti}}(\vec{p}, t = \infty)|^2 \sin\theta d\theta d\phi. \quad (38)$$

Note that for convergent simulations, the total ionization probability is unique for an applied laser pulse, but the value of probability density $\partial \mathcal{P}/\partial \epsilon$ may depend on the grids used. Another interested quantity is the ionization probability density along the polarization direction,

$$\mathcal{P} = \int \frac{\partial \mathcal{P}}{\partial p_\parallel} dp_\parallel, \quad \frac{\partial \mathcal{P}}{\partial p_\parallel} = \int \frac{\partial^2 \mathcal{P}}{\partial p_\parallel \partial p_\perp} dp_\perp. \quad (39)$$

In the tunneling ionization regime, the probability density $\partial \mathcal{P}/\partial p_\parallel$ is regarded as dominant in small $p_\parallel$ [25–27].

## IV. APPLICATION TO INTENSE SHORT LASER PULSE ON HYDROGEN ATOM

We study the laser pulse on hydrogen atom instead of other SAE atoms, mainly because there are no electron-electron effects as for other SAE atoms and, hence, the properties of $\mathcal{P}$-TDSE can be clearly explored. We present results of a Gaussian pulse on hydrogen atom with FWHM $= \sigma$ and carrier frequency $\omega$. So the forms of the electric field and vector potential pulses are

$$\vec{E}(t) = \hat{z}\, E_{\max} e^{-2(\ln 2)(t/\sigma)^2} \sin(\omega t), \quad \vec{A}(t) = -\int_{-\frac{T}{2}}^{t} \vec{E}(t') dt'. \quad (40)$$

To simulate the vanishing of pulse tails at $t = \mp\infty$, we take the ratio $E(t = \mp T/2)/E_{\max}$ to be $10^{-6}$. Thus, the pulse duration $T = \sigma\sqrt{6}\sqrt{2\ln 10/\ln 2} \sim 6.314\,\sigma$. Figure 2 shows an example for the profiles of the field and vector potential at peak intensity $I_0 = 200$ TW/cm$^2$, FWHM of 10 fs, and wavelength of 800 nm. We will focus on the two prominent phenomena of an atom under an intense laser pulse, namely the ATI and the HHG. Applications of present method to other strong field processes are left for future study.

### A. Above-threshold ionization

In Table III we list the parameters of hydrogen atom under the interaction of a Gaussian laser pulse with FWHM 5 fs and 10 fs and peak intensity from 75 to 400 TW/cm$^2$ at 800 nm. $U_p = \sqrt{I_0/4\omega^2}$ denotes the ponderomotive energy. The HHG cut-off order $N_c = (I_p + 3.17U_p)/\omega$ from the tunneling mechanism is also displayed. $\gamma = \sqrt{I_p/2U_p}$ is known as the Keldysh parameter. The parameter $\gamma > 1$ case

TABLE III. Parameters of hydrogen atom under a Gaussian laser pulse of peak intensity 75 to 400 TW/cm$^2$. The carrier wavelength is 800 nm, and FWHM are 5 fs and 10 fs, respectively.

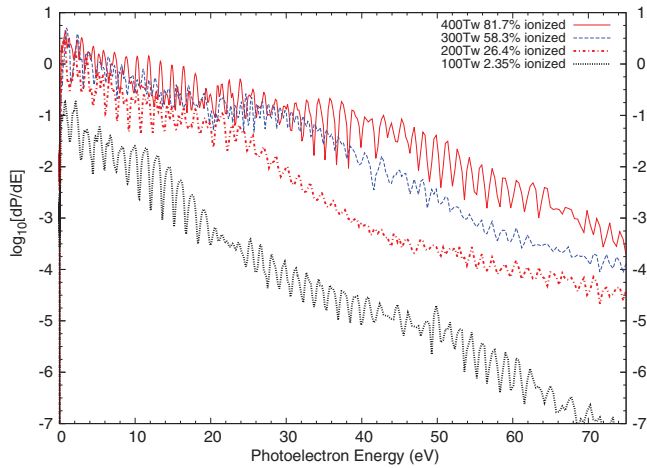| Peak intensity | Keldysh $\gamma$ | $U_p$ (eV) | Ionization (5 fs) | Ionization (10 fs) | HHG cut-off order $N_c$ |
|---|---|---|---|---|---|
| 75 TW/cm$^2$ | 1.232 | 4.48 | 0.47% | 0.93% | 18 |
| 100 TW/cm$^2$ | 1.067 | 5.97 | 1.2% | 2.35% | 21 |
| 200 TW/cm$^2$ | 0.754 | 11.95 | 12.7% | 26.4% | 33 |
| 300 TW/cm$^2$ | 0.616 | 17.92 | 34.5% | 58.3% | 45 |
| 400 TW/cm$^2$ | 0.533 | 23.9 | 59.7% | 81.7% | 57 |

FIG. 3. (Color online) ATI spectra for hydrogen atom under a Gaussian pulse of FWHM 10 fs, 800 nm. The peak intensities are 100, 200, 300, and 400 TW/cm$^2$, respectively.

was regarded as the multiphoton ionization regime and $\gamma < 1$ as the tunneling ionization regime. From the data in Table III, for $\gamma \geqslant 1$, the ionization probability is rather small and, hence, unlike the inert gas atoms [25–27]; the hydrogen target is not useful to study the change of ionization probability density near $p_\parallel \sim 0$ on entering the tunneling regime of $\gamma \leqslant 1$ in Eq. (37). We plot in Fig. 3 the ATI spectra for peak intensity from 100 to 400 TW/cm$^2$ with FWHM of 10 fs and wavelength of 800 nm, where the ionization probability runs from 2.4% to 82%. And we plot the corresponding two-dimensional momentum space photoelectron angular distributions (PAD) in Fig. 4. In the ATI spectra, the ionization density in vertical axis is in logarithmic scale, and the photoelectron kinetic energy in

horizontal axis is in electron volt. We observe the ATI peaks stepped at photon energy (1.55 eV) and ATI peaks switching to high energy from low intensity to high intensity. The kinetic energy up to $\sim 12 U_p$ for 100 TW/cm$^2$ and to $\sim 3 U_p$ for the 400 TW/cm$^2$ case are shown. The ionization density runs over 7 decades. This kind of strong intensity and high ionization probability case is hard to calculate by use of the $\mathcal{R}$-space method.

Because we expand the wave function in Legendre polynomials, and by the PAD expression Eq. (37), the number of strips in the first ring of PAD shows the angular momentum of the first ATI peak. In Fig. 4 we can see the lowest energy ATI peaks have angular momenta of 5,6,4 and 5 for 100, 200, 300, and 400 TW/cm$^2$, respectively. The color levels are in logarithmic scales, $\mathcal{P}$-TDSE method is capable for the PAD of photoelectron under various laser intensities. The dumbbell shaped PAD in high intensity such as Figs. 4(c) and 4(d) were discussed in Ref. [6]. Here the laser parameters used for calculation are realistic. The pulse shape, wavelength, and pulse duration are modeled to laboratory parameters.

### B. High-order harmonic generations

The HHG occur when electron absorbs energy, driven by laser field and releases photons on recolliding with nucleus. In $\mathcal{R}$-TDSE calculation, HHG is obtained from the dipole function of electron near the nucleus. Due to the large extent of continuous wave function, usually we can put a filter at reasonable distance away from the nucleus so that the computation is feasible [19]. However, the effect of filtered wave function is not considered. In the $\mathcal{P}$-TDSE calculation, we have the complete wave function throughout the time evolution. So we can decompose the dipole function into groups
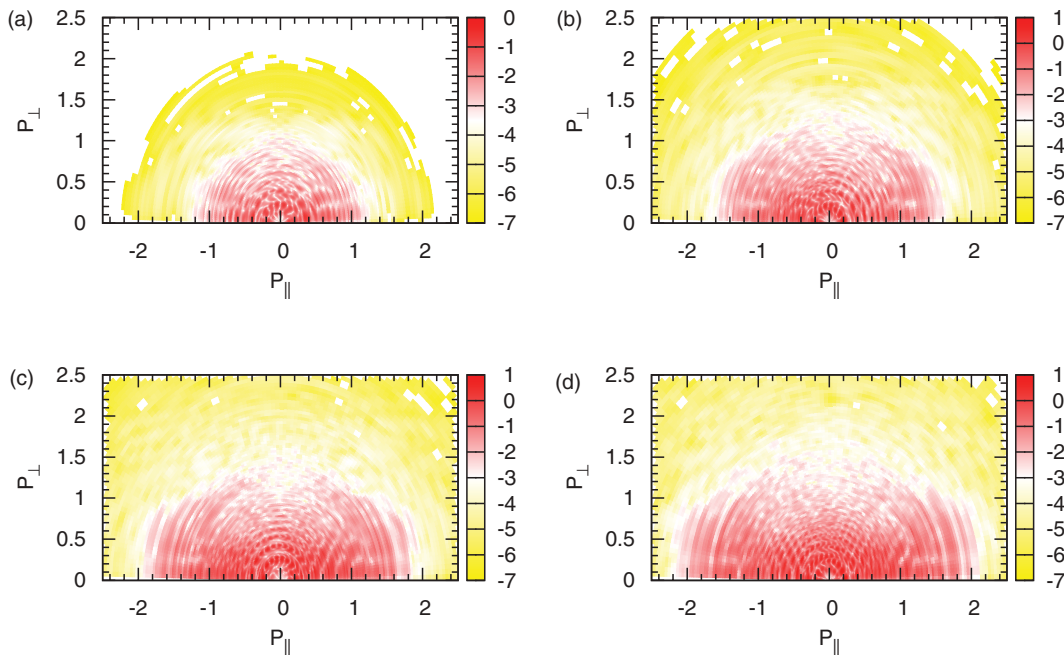


FIG. 4. (Color online) Two-dimensional momentum space photoelectron angular distributions. $p_\parallel$ is the canonical momentum in electric field polarization direction, and $p_\perp$ is vertical to the field polarization. (a) Peak intensity 100 TW/cm$^2$; (b) 200 TW/cm$^2$; (c) 300 TW/cm$^2$; (d) 400 TW/cm$^2$.
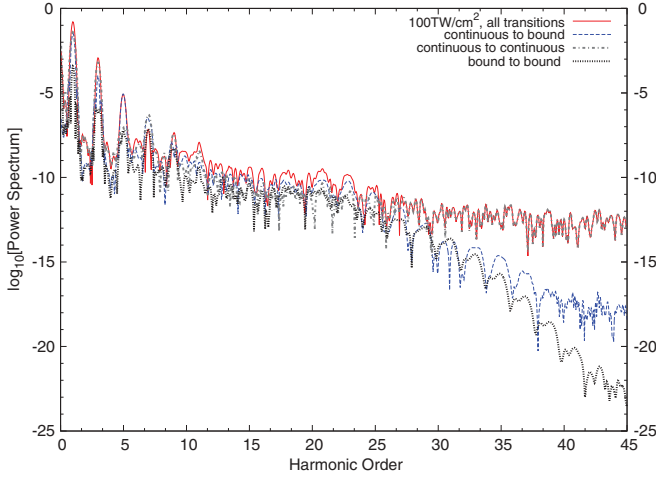
FIG. 5. (Color online) HHG spectrum of hydrogen under a Gaussian pulse of peak intensity 100 TW/cm$^2$, FWHM 10 fs, 800 nm. Red line contains all transitions, dashed blue line contains modeled continuous-bound transitions, gray dash-dot line is for continuous-continuous transitions, and black dotted line is for bound-bound transitions.

of transitions from continuous-continuous, continuous-bound, and bound-bound, respectively as Eq. (35). The problem is that the eigenstates of an atom under laser field, or so called the dressed states, are untractable. We model that during the laser pulse, unperturbed eigenstates with energy larger than the ponderomotive energy ($U_p$) are continuous, and smaller than $U_p$ are bound. Because the major contribution to HHG comes from the time duration inside FWHM, and quiver energy of electron there is in the order of $U_p$. The dipole matrix elements are then classified into the three groups.

Figure 5 shows the HHG spectrum for hydrogen under peak intensity 100 TW/cm$^2$, FWHM 10-fs, 800-nm pulse. Since the Keldysh parameter is 1.07 which is nearly in the tunneling regime, we can use the formula $N_c = I_p + 3.17U_p$ from tunneling concept to estimate the cut-off order, which is 21. We can see that the continuous-bound HHG spectrum simulates the general HHG theory quite well: There is exponential decay for low orders followed by a plateau and then cut-off. The magnitude of bound-bound spectrum is much smaller than contributions from other groups and is negligible. Interestingly, the cut-off behavior is not clearly shown by the spectrum which contains *all* transitions, and the nondecaying high-frequency spectra of all transitions and the continuous-continuous are coincident. It means that the higher-frequency regime spectrum originates from continuous-continuous transitions, and the transitions energies in continuum are no longer stepped by photon energy. The process is not possible to calculate by use of the $\mathcal{R}$-TDSE calculation. With the results, we regard the modeling of HHG here as meaningful. To further examine the use of $U_p$ to decompose the wave function into continuous and bound parts, we show in Fig. 6 the HHG spectra from continuous-bound transitions for the same laser pulse as in Fig. 5. In addition, a simulation uses the instantaneous kinetic energy $A(t)^2/2$ instead of $U_p$ to decompose the continuous and bound states at every time step. We can see both simulate HHG quite well. The main difference happens at harmonics
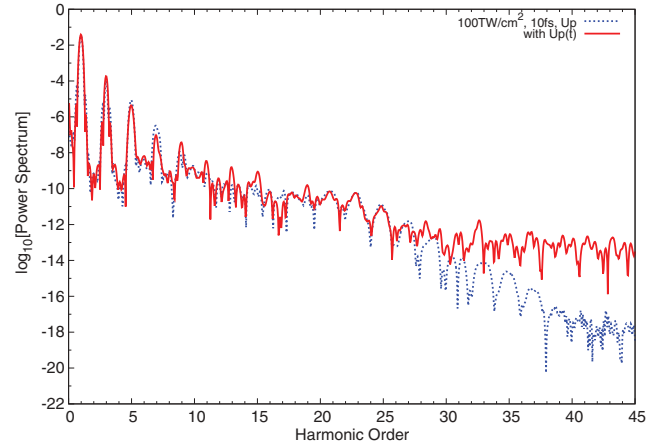
with a frequency higher than the 27th order. The spectrum obtained by using $U_p$ decays much faster than those by using $A(t)^2/2$. But both spectra of this frequency regime are much smaller than the cut-off order 21. Also, a comparison of this $U_p$-decomposed continuous-bound HHG to the $\mathcal{R}$-TDSE [19] for this case was performed. There was not much difference found for the main features and, hence, it was omitted. So, we regard the modeling using $U_p$ as acceptable.

In Fig. 7 we plot the HHG spectra from continuous-bound dipole functions for four intensities from low to very intense. We can see that the HHG spectra show typical characteristics: exponentially decaying low orders and a plateau regime followed by a cut-off regime [20] and the extension of the plateau to higher orders as intensity increased. The cut-off orders $N_c$ from tunneling mechanism are exhibited correctly in the simulations. From the ATI and HHG results shown



FIG. 6. (Color online) Hydrogen HHG spectra from continuous-bound dipole functions, by use of $U_p$ (dotted blue line) and by instantaneous quiver energy $U_p(t) = A^2(t)/2$ (red line), to classify the continuous and bound states. The laser pulse is Gaussian with peak intensity 100 TW/cm$^2$, FWHM 10 fs, 800 nm.
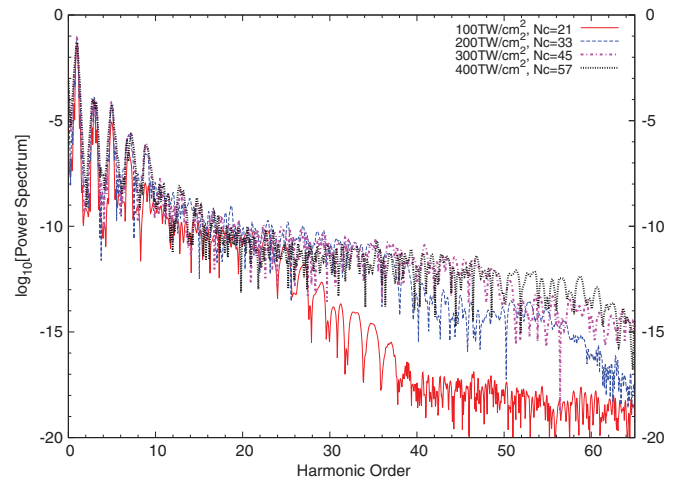


FIG. 7. (Color online) HHG spectra of hydrogen under Gaussian pulses of several peak intensities, FWHM 10 fs, 800 nm. The red line is for 100 TW/cm$^2$, the dashed blue line is for 200 TW/cm$^2$, the dashed-dotted magenta line is for 300 TW/cm$^2$, and the dotted black line is for 100 TW/cm$^2$.

in the paper, we can say that the two important atomic strong-field processes can be calculated well through the present supplementary formulation of the Lande subtraction $\mathcal{P}$-TDSE.

## V. CONCLUSIONS

We derived the supplementary formulation for calculation of the Lande subtraction with finite momentum grids. With this recipe, the use of extremely large momenta is waived and a highly accurate eigenspectrum can be constructed. We demonstrated the applications of this numerical scheme to atoms under intense laser pulses. The two prominent processes, namely the above-threshold ionization and high-order harmonic generations can be simulated in a $\mathcal{P}$-TDSE calculation. We model the continuous and bound parts of a dressed wave function by employing the ponderomotive energy concept. The HHG spectra hence can be decomposed into continuous-continuous, continuous-bound, and bound-bound transitions. The continuous-bound contributes to the $\mathcal{R}$-TDSE HHG results, while continuous-continuous contributes to the higher-frequency continuous spectrum, which has not been calculated by use of the $\mathcal{R}$-TDSE method. We aim in this paper to demonstrate that the $\mathcal{P}$-TDSE method with our recipe can serve as a practical tool for strong-field problems. Other interested strong-field attosecond processes will be studied by use of this method in the future.

## ACKNOWLEDGMENTS

[1] V. A. Fock, Z. Phys. **98**, 145 (1935).

[2] H. A. Bethe and E. E. Salpeter, *Quantum Mechanics of One- and Two-Electron Atoms* (Plenum, New York, 1977).

[3] Y. Rae Kwon and F. Tabakin, Phys. Rev. C **18**, 932 (1978).

[4] J. W. Norbury, K. M. Maung, and D. E. Kahana, Phys. Rev. A **50**, 2075 (1994).

[5] A. Tang and J. W. Norbury, Phys. Rev. E **63**, 066703 (2001).

[6] Z. Zhou and Shih-I Chu, Phys. Rev. A **83**, 013405 (2011).

[7] I. A. Ivanov and J. Mitroy, Comp. Phys. Commun. **134**, 317 (2001).

[8] T. Brabec and F. Krausz, Rev. Mod. Phys. **72**, 545 (2000).

[9] F. Krausz and M. Ivanov, Rev. Mod. Phys. **81**, 163 (2009).

[10] Ue-Li Pen and T. F. Jiang, Phys. Rev. A **53**, 623 (1996).

[11] T. F. Jiang, Comp. Phys. Commun. **178**, 571 (2008).

[12] S. Flügge, *Practical Quantum Mechanics* (Springer-Verlag, New York, 1974), Problems 77 and 78.

[13] B. H. Bransden and C. J. Joachain, *Physics of Atoms and Molecules*, 2nd ed. (Prentice Hall, New York, 2003), Appendix 5.

[14] H. B. Dwight, *Tables of Integrals and Other Mathematical Data*, 4th ed. (Macmillan, New York, 1966), Eqs. 48.12, 702, 735.1.

[15] A. Sarsa, F. J. Gálvez, and E. Buendía, At. Data Nucl. Data Tables **88**, 163 (2004).

[16] X. M. Tong and C. D. Lin, J. Phys. B **38**, 2593 (2005).

[17] J. Wang, Shih-I Chu, and C. Laughlin, Phys. Rev. A **50**, 3208 (1994).

[18] M. R. Hermann and J. A. Fleck, Jr., Phys. Rev. A **38**, 6000 (1988).

[19] T. F. Jiang and Shih-I Chu, Phys. Rev. A **46**, 7322 (1992).

[20] M. Lewenstein, Ph. Balcou, M. Y. Ivanov, Anne L'Huillier, and P. B. Corkum, Phys. Rev. A **49**, 2117 (1994).

[21] P. B. Corkum, Phys. Rev. Lett. **71**, 1994 (1993).

[22] K. C. Kulander, K. J. Schafer, and J. L. Krause, *Super-Intense Laser-Atom Physics* (Plenum, New York, 1993), p. 95.

[23] D. G. Arbó, J. E. Miraglia, and M. S. Gravielle, K. Schiessl, Emil Persson, and J. Burgdörfer, Phys. Rev. A **77**, 013401 (2008).

[24] Jingtao Zhang and Takashi Nakajima, Phys. Rev. A **77**, 043417 (2008).

[25] R. Moshammer *et al.*, Phys. Rev. Lett. **91**, 113002 (2003).

[26] M. Wickenhauser, X. M. Tong, D. G. Arbó, J. Burgdörfer, and C. D. Lin, Phys. Rev. A **74**, 041402(R) (2006).

[27] M. Abu-Samha and L. B. Madsen, J. Phys. B **44**, 235601 (2011).